

Supplementary Materials for

Spontaneous weathering of natural minerals in charged water microdroplets forms nanomaterials

B. K. Spoorthi et al.

Corresponding author: Thalappil Pradeep, pradeep@iitm.ac.in

Science **384**, 1012 (2024) DOI: 10.1126/science.adl3364

The PDF file includes:

Materials and Methods Supplementary Text Figs. S1 to S10 Tables S1 to S7 References

Other Supplementary Material for this manuscript includes the following:

Movie S1

Materials and Methods

Materials

River sand and natural ruby were purchased from the local market and fused alumina (99+%) was purchased from Sigma-Aldrich. All samples were used without additional purification. Ultrapure water (18.5 M Ω Milli Q) was used for all the experiments. The samples were ground using a laboratory mortar and pestle and suspended in water and centrifuged using a Remi RM-03 plus centrifuge. Prior to centrifugation, the particle suspension was ultrasonicated (Digital ultrasonic cleaner, 40 kHz, 100 W) for 10 min to ensure the separation of particles.

Characterization

Photographs of the initial samples were taken using a digital single-lens reflex (DSLR) camera. Optical images of the micron-sized particles were captured by VH-Z100R Keyence optical microscope. Thermo Scientfic Verios G4 UC high-resolution FESEM at 20 kV accelerating voltage was used to study the surface morphology of the micron-sized particles. Energy dispersive spectroscopy (EDS), using FESM confirmed their composition. Thin film of gold was sputtered on the sample to reduce charging. High-resolution TEM images of the nanostructures were taken at an accelerating voltage of 200 kV using a JEOL 3010 instrument. The sizes of the materials were compared by performing thin-film X-ray diffraction using Rigaku SmartLab X-ray diffractometer system with Cu K α radiation (λ = 1.5406 Å). Raman spectra were recorded using a CRM alpha 300 S spectrometer of Witec, Germany, with an excitation source of 532 nm. The mass spectral data were acquired using a Thermo Scientific LTQ XL mass spectrometer.

Electrospray deposition experiments

A home-built electrospray set-up was used for microdroplet experiments (Fig. 1A). The spray was generated from a Hamilton syringe which was connected to a silica capillary of 50 µm inner diameter through a union connector. The syringe needle was connected to a high voltage power source. A syringe pump controlled the flow rate of the suspension. The substrate was grounded. The experiment was done under ambient conditions (25 °C, 50-60% relative humidity). A multinozzle set-up was prepared to scale up the method. The components used such as silica capillaries were purchased from Molex, USA. Union connectors and PEEK tubing sleeves were procured from IDEX Health & Science, USA.

Determining the collection yield of the sample

The spray was carried out (as mentioned in the experimental section) at the optimized condition. Initially weight of the bare substrate (aluminum) was taken. Subsequently, the fine suspension of silica was electrosprayed. After the electrospray, the weight of the substrate with the sample was measured. The difference in the weight before and after deposition gives the weight of the silica deposited. The ratio of the sprayed sample with respect to the initial sample gives the collection yield.

Computational details

Our first-principles calculations are based on density functional theory as implemented in QUANTUM ESPRESSO (14), and ultrasoft pseudopotentials to model interactions between valence electrons and the ionic cores. We used a generalized-gradient approximation (GGA) (15) of the exchange-correlation energy with a revised functional PBEsol parameterized by Perdew,

Burke and Ernzerhof (PBE) (16). Electronic wave functions and charge density expansions in plane wave basis sets were truncated at cut-off energies of 30 Ry and 240 Ry respectively. We analyze here bulk and a slab terminated with (110) surfaces of SiO₂, since the TEM images in experiments confirm the (110) surface of quartz or SiO₂. A 1x2x4 supercell is used to model the slab with (110) surfaces by introducing a vacuum layer of 15 Å thickness parallel to the slab separating its adjacent periodic images. Brillouin Zone (BZ) integrations were sampled on uniform 12x12x8 and 2x1x1 meshes of k-points for bulk and slab of SiO₂, respectively. Calculated lattice constants of bulk SiO₂ (a=4.95 Å and c=5.44 Å) are within the typical GGA errors with respect to their experimental estimates ((a=4.95 Å and c=5.44 Å) (17). To simulate responses of the slab to electric field, we add a saw-tooth potential as a function z. Calculations were also performed on the (001) surface of SiO₂ to confirm the conclusion drawn. Similar calculations were conducted on the (001) surface of α -Al₂O₃ (alumina). Additional details are presented in the main text as well as in Tables S2-S5.

Supplementary figures

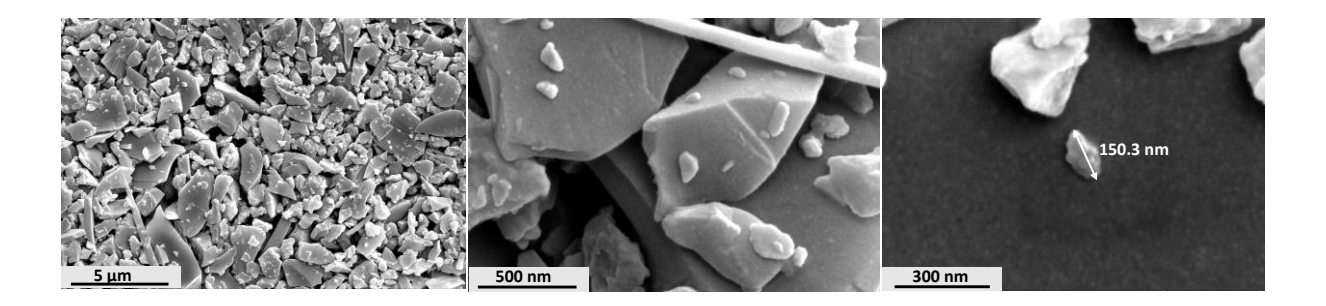


Fig. S1. FESEM images of silica particles before electrospray, at various magnifications, showing that smaller adhering particles are larger than 100s of nm in size.

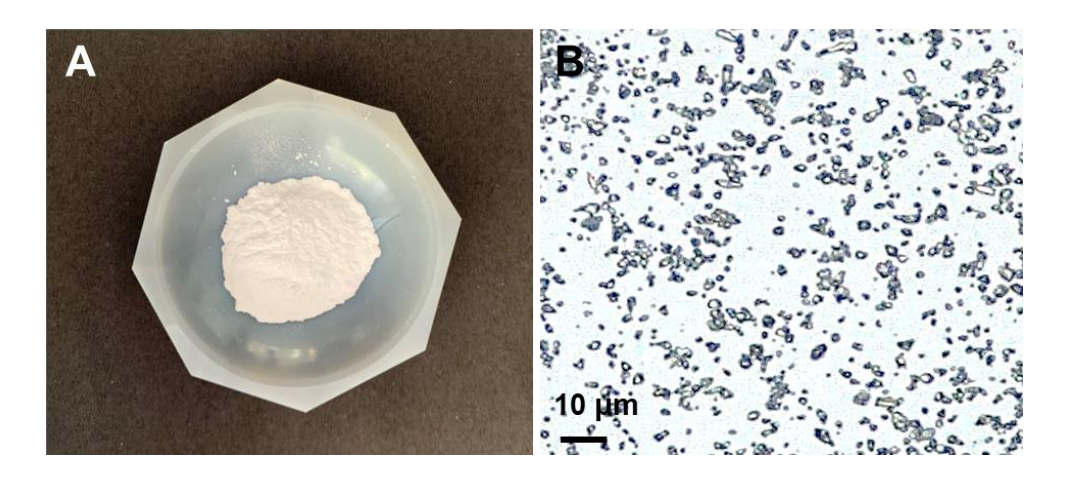


Fig. S2. Images of natural quartz. (A) Photograph of the ground quartz powder used for centrifugation and separation of smaller particles. (B) Optical image of the particles separated by centrifugation and used for electrospray; particles are below 10 um in size.

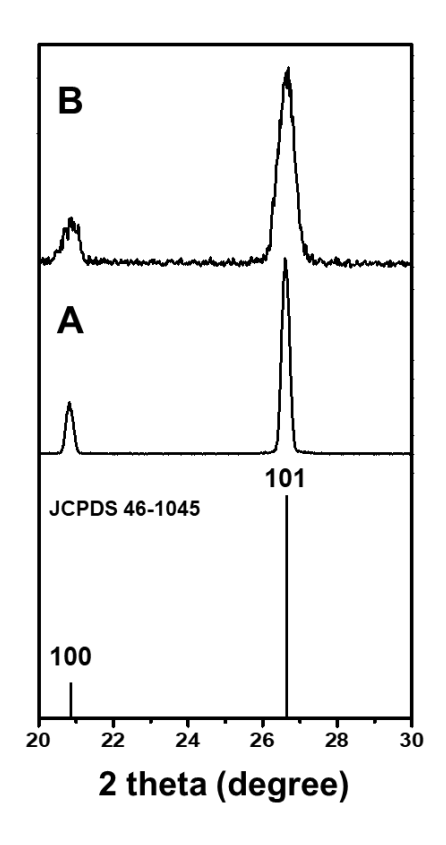


Fig. S3. Detecting nanoparticles in bulk form. XRD of ground natural quartz before (A) and after (B) electrospray deposition, compared with the JCPDS data of quartz. Broadened peaks in (B) indicate the smaller size of the quartz particles.

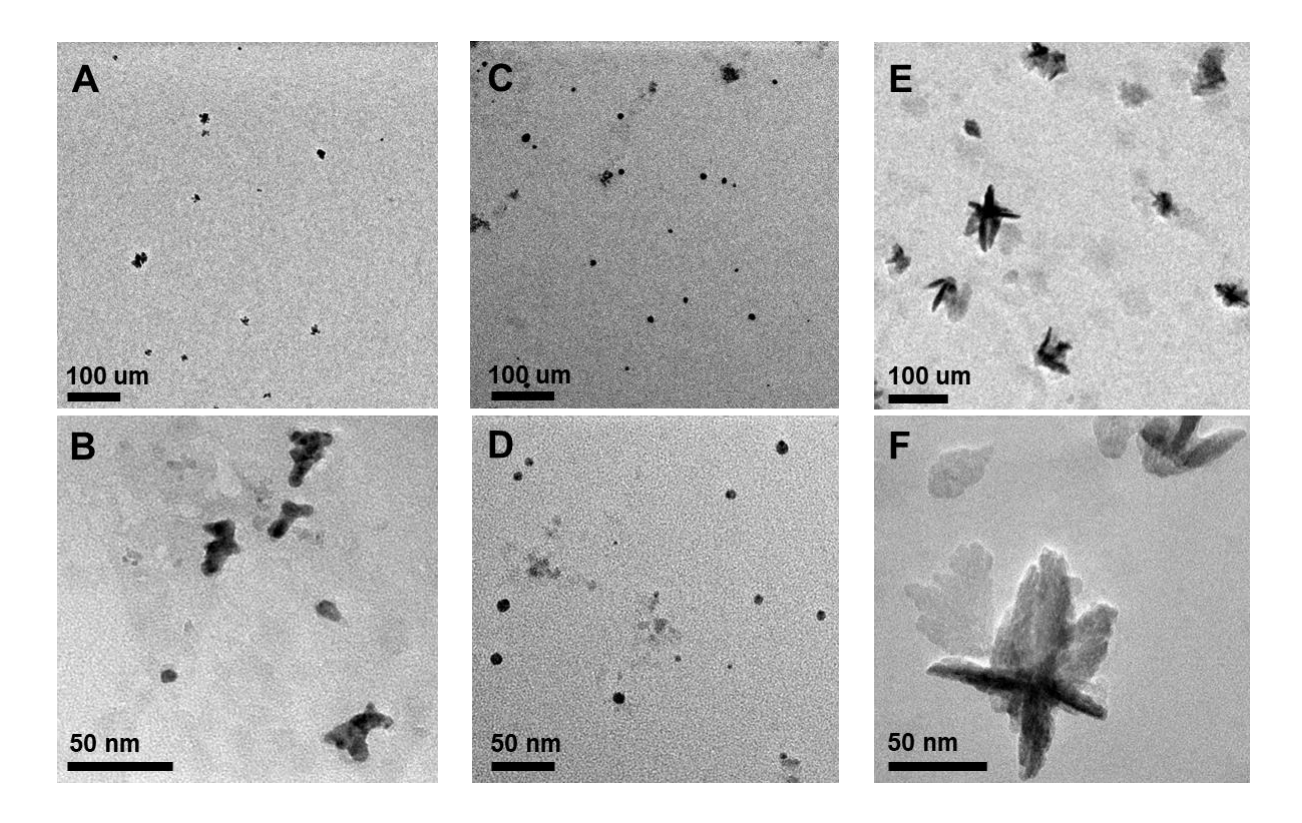


Fig. S4. Effect of spray potential on the particles. HRTEM images of natural quartz at various applied spray potentials (A, B) 3.0 kV where the fragmentation just begins. (C, D) 4.5 kV. (E, F) 5.5 kV.

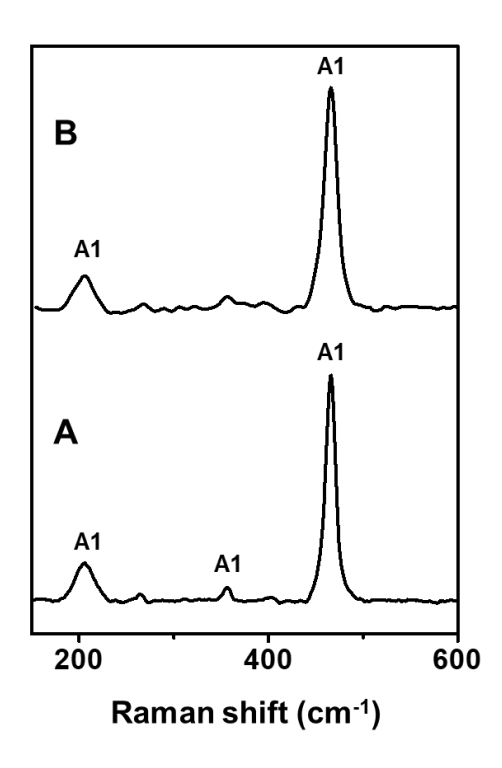


Fig. S5. Raman spectroscopic characterization. Raman spectra showing the characteristic Si-O symmetric stretch (A_1) of natural quartz. (A) Before and (B) after electrospray deposition. Peaks confirm the structural integrity of quartz. The spectra were collected with 532 nm excitation.

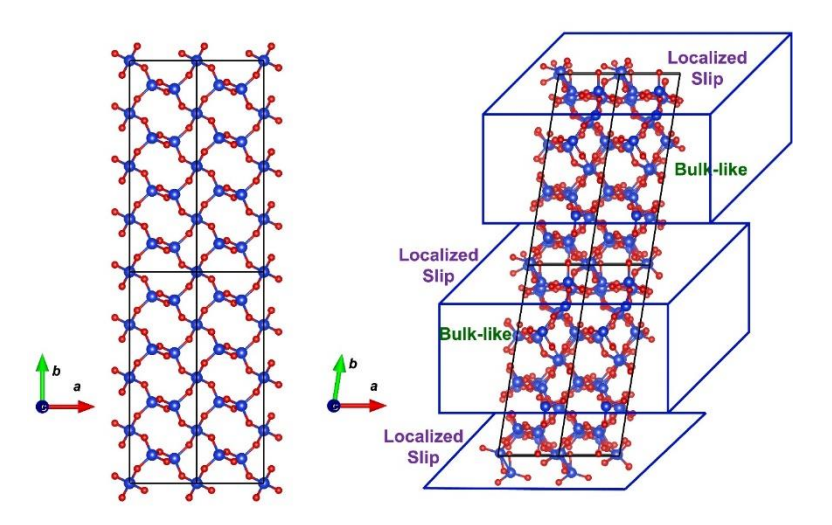


Fig. S6. Illustration of slip. Schematic representation showing 'no slip' and 'slip' representation of SiO₂. The slip has been introduced in the crystal using the transformation equation as shown in the figure.

Table S1: The generalized SFEs calculated for (110) surface of bulk and slab SiO_2 with (0, 0), (0, 0.5), (0.5, 0) and (0.5, 0.5) slip configurations.

	х	Z	Slab	Bulk
SFE (J/	0.0	0.0	0.0	0.0
m^2)	0.5	0.5	-1.21	2.08
ŕ	0.5	0.0	1.20	1.65
	0.0	0.5	-0.07	1.73

Table S2: Calculated cleavage energies (in J/m^2) along the (010) direction for the (001) surface of bulk and slab SiO₂.

Vacuum thickness (Å)	Bulk	Slab
0	0	0
8	5.84	4.53

Here we have simulated the processes of cleavage and slip in bulk and (001) terminated slab of SiO_2 . We obtained energies of cleavage of bulk and slab of SiO_2 as a function of vacuum thickness, b and find that cleavage energies of the slab are ~20% lower than that of the bulk (see above), supporting our suggestion that breaking of a nanoscale crystal of SiO_2 across (001) surface is easier compared to the bulk.

Table S3: Generalized SFEs calculated for (001) surface of SiO_2 slab with (0, 0), (0, 0.5), (0.5, 0) and (0.5, 0.5) slip configurations.

	х	Z	Slab
SFE (J/	0.0	0.0	0.0
m^2)	0.5	0.5	-0.32
	0.5	0.0	0.94
	0.0	0.5	1.13

Here we examine the formation of nanocrystals through nucleation of a stacking fault on (010) plane with slip localized at a single (010) plane, achieved with transformation of the unit cell vector \vec{b} using

$$\vec{f} = x\vec{a} + \vec{b} + z\vec{c},$$

where \vec{a} , \vec{b} and \vec{c} are the periodic cell vectors, and $(x, z \in [0,1])$ are the fractional coordinates. Negative SFE of (0.5, 0.5) slip on (010) plane in the (001) slab of SiO₂ relative to the reference structure (x, z) = (0, 0) means spontaneous formation of stacking faults (see above), which is similar to what we reported for the (110) surface of SiO₂. We therefore conclude that these mechanisms of nanocrystal formation in SiO₂ are generic and can happen along other surfaces also.

Table S4: Calculated cleavage energies (in J/m^2) along the (010) direction for the (001) surface of bulk and slab of Al_2O_3 .

Vacuum thickness (Å)	Bulk	Slab
0	0	0
8	7.43	7.30

The simulations of the stable form α -Al₂O₃ (alumina), the corundum structure ($R\overline{3}c$ space group) are presented here. Our estimates of optimized lattice parameters, $\alpha = 5.14$ Å and $\alpha = 55.35^{\circ}$ are within the typical GGA errors of their experimental values ($\alpha = 5.13$ Å and $\alpha = 55.33^{\circ}$) [14]. Simulation was performed by (a) subjecting the crystal to uniaxial tensile strain localized at a (010) plane, and (b) slip on a (010) plane. We find that cleavage energy of the slab is lower than that of bulk.

Table S5: SFEs of the (010) plane with (0, 0), (0, 0.5), (0.5, 0) and (0.5, 0.5) slip configurations on the (001) surface of neutral and positively charged slab of Al_2O_3 .

	х	Z	Neutral Slab	Positive Slab
SFE (J/	0.0	0.0	0.0	0.0
m^2)	0.5	0.5	1.86	1.75
	0.5	0.0	2.51	-0.27
	0.0	0.5	1.85	-0.21

Generalized SFEs of four configurations of slip on (010) plane have been tabulated here. Positive SFE in neutral slab of α -Al₂O₃ indicate formation of slip in alumina is not quite favorable. To understand the process of disintegration of alumina in nanoforms, a charged system was simulated by removing an electron and adding a compensating jellium to maintain charge neutrality of the periodic system. The SFEs in charged alumina are negative for the slips at = (0.5, 0.0) and (0.0, 0.5) configurations, supporting spontaneous formation of stacking faults, facilitated by interaction with protons

Table S6. SFEs of (010) direction with (0, 0), (0, 0.5), (0.5, 0) and (0.5, 0.5) slip configurations on the (110) plane of SiO_2 from our DFT-based calculations analyzing the effects of hydrogen atom (H-atom) and electric field ($E = 10^8 \ V/m$). Our calculations show that SFEs in slab-SiO₂ with (0, 0.5) and (0.5, 0.5) configurations are negative and energetically favorable (marked in bold). The SFEs for bulk remain positive.

	Slab					
SFE (1/	х	Z	w/o H- atom	1 H- atom	2 H- atoms	E
$ \begin{array}{c c} SFE (J/\\ m^2) \end{array} $	0.0	0.0	0	0	0	0
	0.5	0.5	-1.21	-0.93	-0.88	-1.20
	0.5	0.0	1.20	1.18	0.90	1.12
	0.0	0.5	-0.07	0.89	-0.83	-0.09

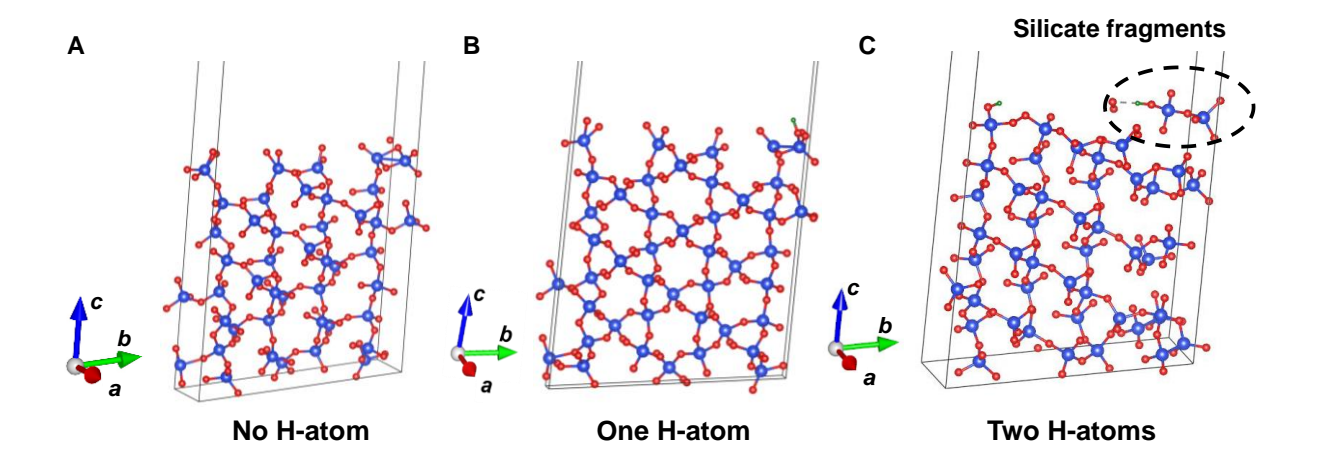


Fig. S7. Silicate formation upon interaction with H atoms. The relaxed stacking fault structures with a slip vector (x,z) = (0,0.5) (A) without hydrogen atom, (B) with one hydrogen atom and (C) two hydrogen atoms, clearly highlighting surface reconstruction and formation of silicate fragments in (0,0.5) stacking fault structure with two hydrogen atoms. Silicon atoms are shown in blue, oxygen atoms in red, and hydrogen atoms in green. Hydrogen atoms are shown also with dotted arrows.

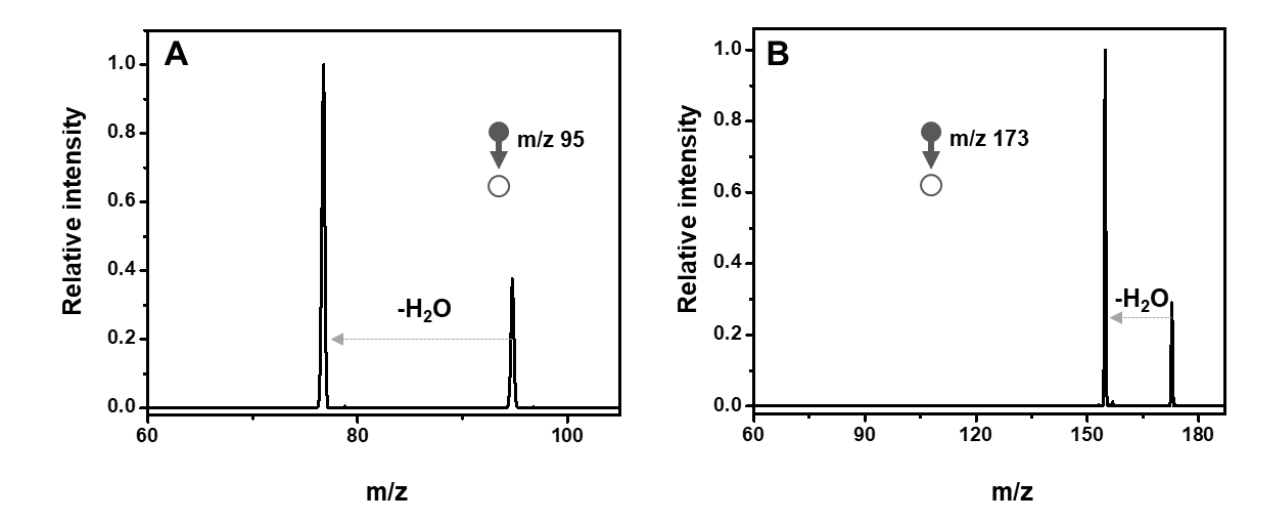


Fig. S8. Confirming the composition of ions in the gas phase. Tandem mass spectra of standard silica solution. (a) and (b) showing the water loss during fragmentation of m/z 95 [SiO₃H.H₂O]⁻ and m/z 173 [Si₂O₆H₃.H₂O]⁻, respectively.

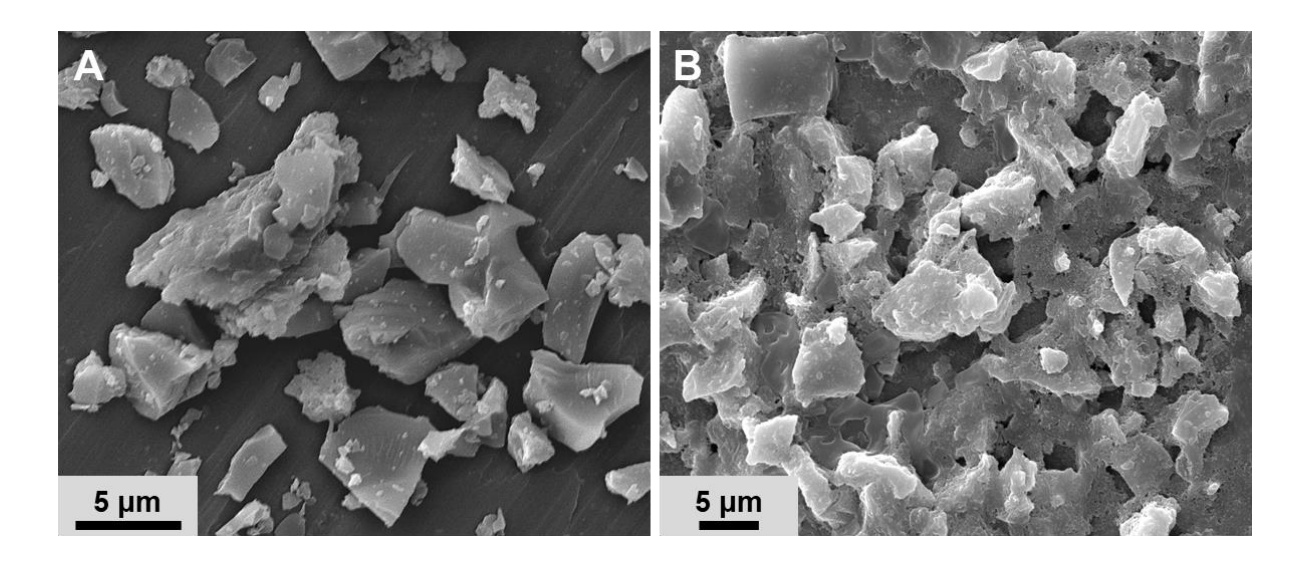


Fig. S9. Effect of charged microdroplets on quartz. FESEM images of natural quartz before (A) and after (B) deposition of charged microdroplets. Pure water was electrosprayed under conditions shown in Fig. 1A, onto an aluminum substrate covered with mineral particles for 4 h and the resulting substrate with minerals was analyzed. Increased surface roughness is seen in the product particles.

Table S7: Generalized SFEs calculated for (110) surface of positively charged slab of SiO_2 with slips (0, 0), (0, 0.5), (0.5, 0) and (0.5, 0.5) on the (010) plane.

	x	Z	Slab
SFE (J/	0.0	0.0	0.0
m^2)	0.5	0.5	-1.18
	0.5	0.0	0.81
	0.0	0.5	0.03

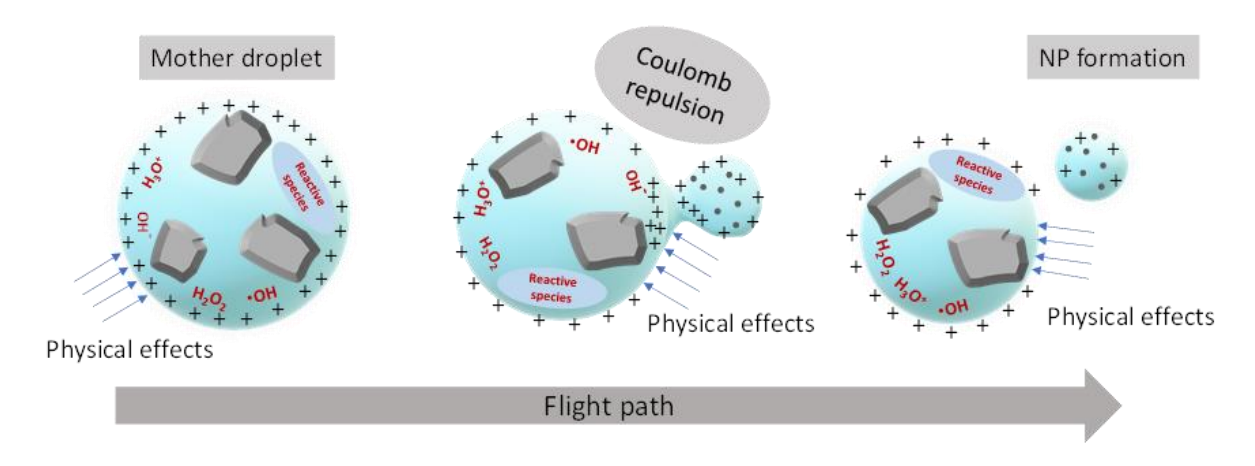


Fig. S10. Illustration of the process. Schematic representation of the mechanism of NP formation.

Movie S1: A detailed video of the experiment demonstrating the spontaneous weathering of natural minerals in charged water microdroplets.

References and Notes

- M. F. Hochella Jr., D. W. Mogk, J. Ranville, I. C. Allen, G. W. Luther, L. C. Marr, B. P. McGrail, M. Murayama, N. P. Qafoku, K. M. Rosso, N. Sahai, P. A. Schroeder, P. Vikesland, P. Westerhoff, Y. Yang, Natural, incidental, and engineered nanomaterials and their impacts on the Earth system. *Science* 363, eaau8299 (2019). doi:10.1126/science.aau8299 Medline
- 2. Z. Wei, Y. Li, R. G. Cooks, X. Yan, Accelerated reaction kinetics in microdroplets: Overview and recent developments. *Annu. Rev. Phys. Chem.* **71**, 31–51 (2020). doi:10.1146/annurev-physchem-121319-110654 Medline
- 3. J. K. Lee, S. Kim, H. G. Nam, R. N. Zare, Microdroplet fusion mass spectrometry for fast reaction kinetics. *Proc. Natl. Acad. Sci. U.S.A.* **112**, 3898–3903 (2015). doi:10.1073/pnas.1503689112 Medline
- 4. A. Wortmann, A. Kistler-Momotova, R. Zenobi, M. C. Heine, O. Wilhelm, S. E. Pratsinis, Shrinking droplets in electrospray ionization and their influence on chemical equilibria. *J. Am. Soc. Mass Spectrom.* **18**, 385–393 (2007). doi:10.1016/j.jasms.2006.10.010 Medline
- 5. D. Sarkar, A. Mahapatra, A. Som, R. Kumar, A. Nagar, A. Baidya, T. Pradeep, Patterned nanobrush nature mimics with unprecedented water-harvesting efficiency. *Adv. Mater. Interfaces* 5, 1800667 (2018). doi:10.1002/admi.201800667
- 6. H. Wei, E. P. Vejerano, W. Leng, Q. Huang, M. R. Willner, L. C. Marr, P. J. Vikesland, Aerosol microdroplets exhibit a stable pH gradient. *Proc. Natl. Acad. Sci. U.S.A.* **115**, 7272–7277 (2018). doi:10.1073/pnas.1720488115 Medline
- 7. L. Qiu, N. M. Morato, K.-H. Huang, R. G. Cooks, Spontaneous water radical cation oxidation at double bonds in microdroplets. *Front Chem.* **10**, 903774 (2022). doi:10.3389/fchem.2022.903774 Medline
- 8. D. Zhang, X. Yuan, C. Gong, X. Zhang, High electric field on water microdroplets catalyzes spontaneous and ultrafast oxidative C-H/N-H cross-coupling. *J. Am. Chem. Soc.* **144**, 16184–16190 (2022). doi:10.1021/jacs.2c07385 Medline
- 9. M. S. Krivokorytov, A. Y. Vinokhodov, Y. V. Sidelnikov, V. M. Krivtsun, V. O. Kompanets, A. A. Lash, K. N. Koshelev, V. V. Medvedev, Cavitation and spallation in liquid metal droplets produced by subpicosecond pulsed laser radiation. *Phys. Rev. E* **95**, 031101 (2017). doi:10.1103/PhysRevE.95.031101 Medline
- 10. S. Banerjee, S. Mazumdar, Electrospray ionization mass spectrometry: A technique to access the information beyond the molecular weight of the analyte. *Int. J. Anal. Chem.* **2012**, 282574 (2012). doi:10.1155/2012/282574 Medline
- 11. P. Basuri, A. Chakraborty, T. Ahuja, B. Mondal, J. S. Kumar, T. Pradeep, Spatial reorganization of analytes in charged aqueous microdroplets. *Chem. Sci.* **13**, 13321–13329 (2022). doi:10.1039/D2SC04589C Medline
- 12. F. Sicard, J. Toro-Mendoza, A. Striolo, Nanoparticles actively fragment armored droplets. *ACS Nano* **13**, 9498–9503 (2019). doi:10.1021/acsnano.9b04454 Medline

- 13. Z. Tang, S. Lin, Z. L. Wang, Quantifying contact-electrification induced charge transfer on a liquid droplet after contacting with a liquid or solid. *Adv. Mater.* **33**, e2102886 (2021). doi:10.1002/adma.202102886 Medline
- 14. Quantum-ESPRESSO is a community project for high-quality quantum-simulation software based on density-functional theory and is coordinated by P. Giannozzi. See http://www.quantum-espresso.org and http://www.pwscf.org.
- 15. X. Hua, X. Chen, W. A. Goddard III, Generalized generalized gradient approximation: An improved density-functional theory for accurate orbital eigenvalues. *Phys. Rev. B Condens. Matter* **55**, 16103–16109 (1997). doi:10.1103/PhysRevB.55.16103
- 16. L. A. Constantin, J. M. Pitarke, J. F. Dobson, A. Garcia-Lekue, J. P. Perdew, High-level correlated approach to the jellium surface energy, without uniform-gas input. *Phys. Rev. Lett.* **100**, 036401 (2008). doi:10.1103/PhysRevLett.100.036401 Medline
- 17. S. M. Antao, I. Hassan, J. Wang, P. L. Lee, B. H. Toby, State-of-the-art high-resolution powder x-ray diffraction (HRPXRD) illustrated with rietveld structure refinement of quartz, sodalite, tremolite, and meionite. *Can. Mineral.* **46**, 1501 (2008). doi:10.3749/canmin.46.5.1501